ACS NANO
Cite This: ACS Nano 2019, 13, 5785−5798
www.acsnano.org

ARTICLE

Elimination Pathways of Nanoparticles

Wilson Poon,[†,‡] Yi-Nan Zhang,[†,‡,◆] Ben Ouyang,[†,‡,§,◆] Benjamin R. Kingston,[†,‡] Jamie L. Y. Wu,[†,‡] Stefan Wilhelm,[∥,⊥] and Warren C. W. Chan[*,†,‡,#,∇,○]

[†]Institute of Biomaterials and Biomedical Engineering, University of Toronto, Toronto, Ontario M5S 3G9, Canada
[‡]Terrence Donnelly Centre for Cellular and Biomolecular Research, University of Toronto, Toronto, Ontario M5S 3E1, Canada
[§]MD/PhD Program, Faculty of Medicine, University of Toronto, Toronto, Ontario M5S 1A8, Canada
[∥]Stephenson School of Biomedical Engineering, University of Oklahoma, Norman, Oklahoma 73019, United States
[⊥]Stephenson Cancer Center, Oklahoma City, Oklahoma 73104, United States
[#]Department of Chemical Engineering and Applied Chemistry, University of Toronto, Toronto, Ontario M5S 3E5, Canada
[∇]Department of Materials Science and Engineering, University of Toronto, Toronto, Ontario M5S 1A1, Canada
[○]Department of Chemistry, University of Toronto, Toronto, Ontario M5S 3H6, Canada

Supporting Information

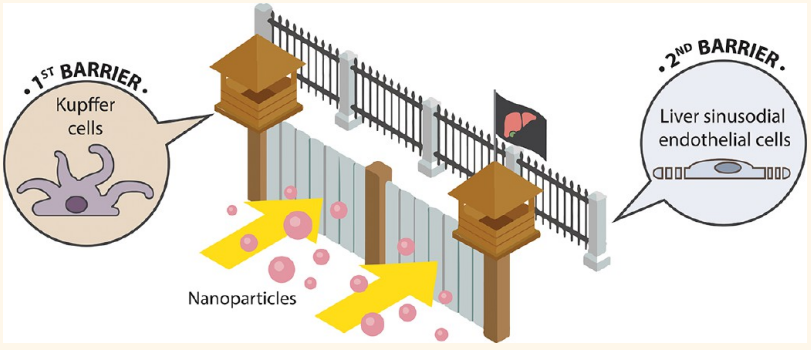

ABSTRACT: **Understanding how nanoparticles are eliminated from the body is required for their successful clinical translation. Many promising nanoparticle formulations for *in vivo* medical applications are large (>5.5 nm) and nonbiodegradable, so they cannot be eliminated renally. A proposed pathway for these nanoparticles is hepatobiliary elimination, but their transport has not been well-studied. Here, we explored the barriers that determined the elimination of nanoparticles through the hepatobiliary route. The route of hepatobiliary elimination is usually through the following pathway: (1) liver sinusoid, (2) space of Disse, (3) hepatocytes, (4) bile ducts, (5) intestines, and (6) out of the body. We discovered that the interaction of nanoparticles with liver nonparenchymal cells (*e.g.*, Kupffer cells and liver sinusoidal endothelial cells) determines the elimination fate. Each step in the route contains cells that can sequester and chemically or physically alter the nanoparticles, which influences their fecal elimination. We showed that the removal of Kupffer cells increased fecal elimination by >10 times. Combining our results with those of prior studies, we can start to build a systematic view of nanoparticle elimination pathways as it relates to particle size and other design parameters. This is critical to engineering medically useful and translatable nanotechnologies.**

KEYWORDS: *nanoparticle, elimination, liver, Kupffer cell, liver sinusoidal endothelial cell, hepatocyte, hepatobiliary*

The fate of nanoparticles is important for regulatory purposes due to concerns about chronic accumulation and patient safety.[1] The United States Food and Drug Administration (FDA) requires nanoparticles that function as pharmaceutical drugs to be metabolized or excreted from the body after their intended medical use.[1,2] Current strategies for nanoparticle elimination rely on their intrinsic biodegradability or small size to be eliminated renally. However, this prevents the clinical use of large, nonbiodegradable, inorganic nanoparticles that have shown great therapeutic potential in areas such as image-guided surgery[3] and photothermal therapy.[4]

Intravenously administered nanoparticles circulate in the blood until they are cleared from circulation and eliminated from the body by two main mechanisms: (i) renal elimination and (ii) hepatobiliary elimination.[5] The renal pathway for nanoparticle elimination is well-characterized. Choi *et al.* showed that quantum dots with a core particle size smaller

Received: February 18, 2019
Accepted: April 16, 2019
Published: April 16, 2019

DOI: 10.1021/acsnano.9b01383
ACS Nano 2019, 13, 5785−5798

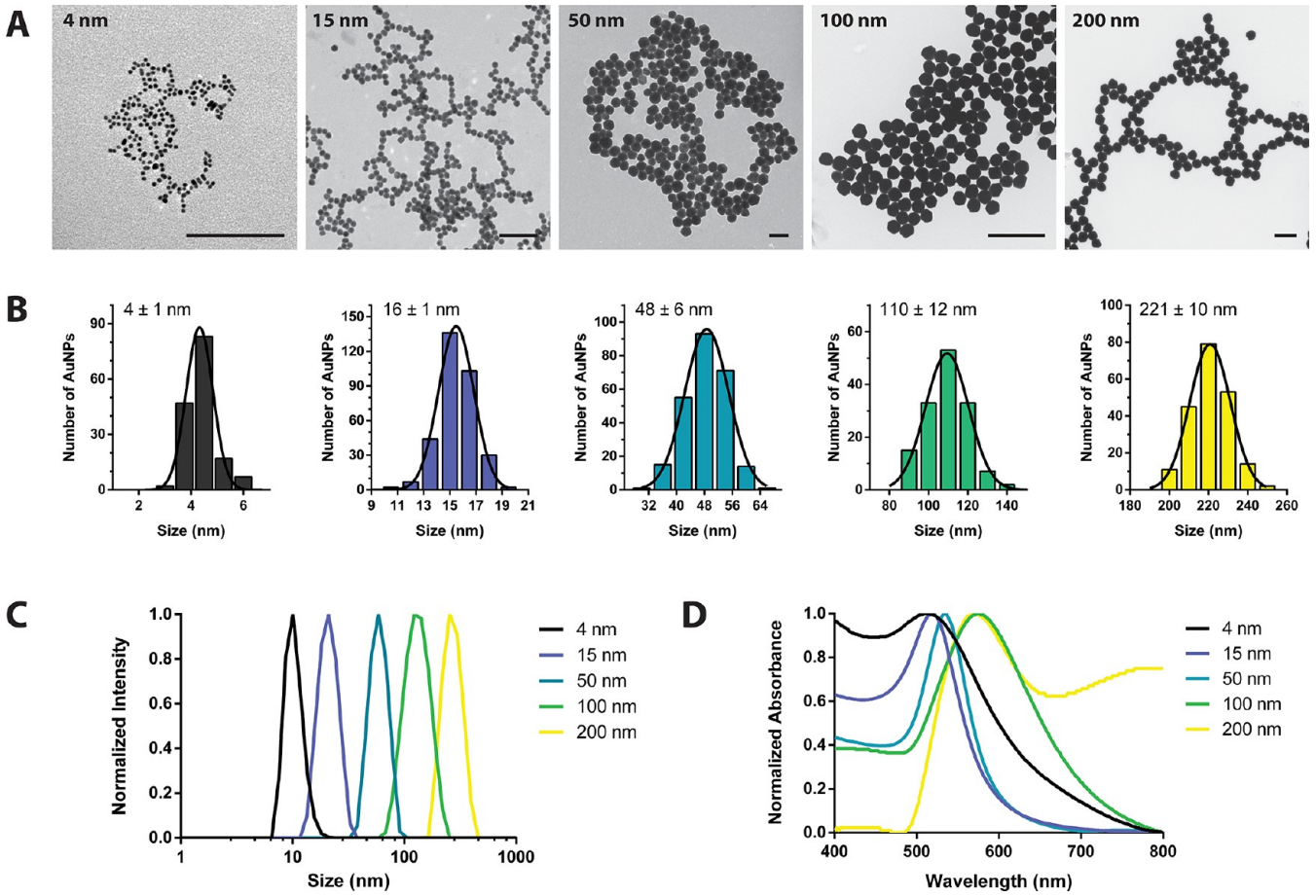

Figure 1. Nanoparticle synthesis and characterization. (A) Transmission electron micrographs of different sized AuNPs; scale bars for the three leftmost micrographs are 100 nm and 500 nm for the two rightmost micrographs. (B) Corresponding histograms and Gaussian fits of the measured AuNP size distribution as determined from their TEM micrographs. (C) Hydrodynamic diameter of different sized AuNPs. (D) Normalized absorbance spectra of different sized AuNPs.

than 5.5 nm diameter undergo efficient urinary excretion due to the pore size limit of glomerular filtration in the kidneys.[6] Many strategies for tuning nanoparticle renal elimination have since been developed from this fundamental understanding using nanoparticle size, core density, surface charge, and surface chemistry.[7,8] Conversely, the principles governing nanoparticle hepatobiliary elimination are relatively unexplored. Some studies suggested that materials can undergo hepatobiliary elimination *via* transcytosis through hepatocytes in the liver, resulting in transport *via* the bile canaliculi into the biliary system, then into the gastrointestinal tract, and eventual elimination in feces.[9,10] Additionally, hepatobiliary elimination of nanoparticles is usually slow, ranging from hours to months or longer.[5] However, the extent and time-scale of hepatobiliary elimination of nanoparticles reported are highly variable due to inconsistent quantification methodologies. Semiquantitative methods for evaluating organ biodistribution and feces using fluorescence imaging and optoacoustic tomography have limited sensitivity and detection lifetimes. Metabolism and elimination studies using radiolabeled nanoparticles can also misrepresent the fate of the nanoparticle inorganic core due to degradation of the radiolabeled organic shell or cleavage of the radiolabel from surface ligands.[11,12] A literature review on nanoparticle hepatobiliary elimination previously showed that intravenously administered nanoparticles of a wide variety of material and chemistry designs span the entire spectrum of elimination efficiencies, ranging from 0% to 100%.[5] Our prior studies showed that quantum dots are not eliminated through the hepatobiliary system.[13] In contrast, spectroscopic and microscopy techniques showed that carbon nanotubes, silica, and lanthanide nanoparticles remained intact in feces after intravenous administration.[14−16]

We sought to understand the discrepancy among prior studies by exploring the biological barriers and mechanism of nanoparticle elimination in this study. We hypothesized that the interaction of liver cells with the nanoparticles in the hepatobiliary pathway dictated their fate and elimination out of the body. These interactions would be determined by nanoparticle size and composition. Here, we identified non-parenchymal liver cells as the main barriers to the hepatobiliary elimination of large, nonbiodegradable, inorganic nanoparticles. Combining our findings with those from literature, we can start to create an *in vivo* decision tree of the relationship between nanoparticle design and elimination pathway. Ultimately, the mapping of the *in vivo* fate provides a guide to engineer eliminable nanoparticles.

RESULTS AND DISCUSSION

The Hepatobiliary Transport Pathway of AuNPs. First, we wanted to map the hepatobiliary elimination route of inorganic nanoparticles. Our previous studies showed that core gold nanoparticles (AuNPs) did not degrade *in vivo*, which

DOI: 10.1021/acsnano.9b01383
ACS Nano 2019, 13, 5785−5798

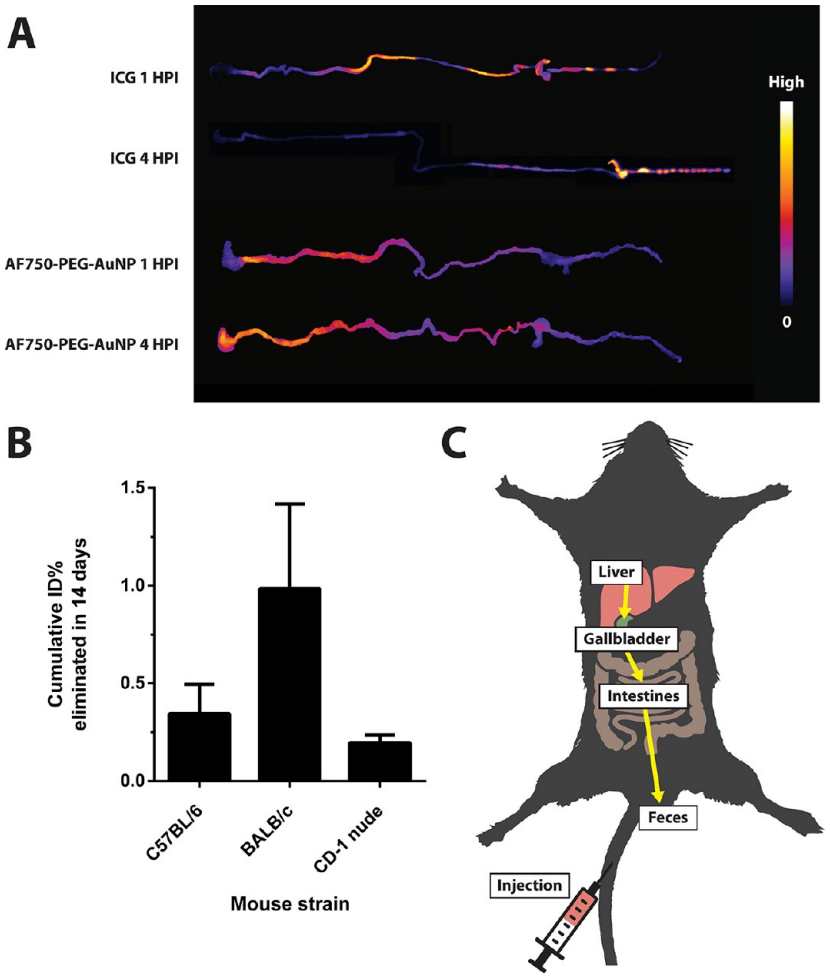

Figure 2. Characterization of nanoparticle hepatobiliary elimination. (A) *Ex vivo* fluorescence imaging of the gastrointestinal tract from BALB/c mice 1 and 4 h post-injection of ICG or AF750-PEG-AuNPs. (B) Quantification of cumulative hepatobiliary elimination of 50 nm AuNPs in feces for 14 days following administration into C57BL/6, BALB/c, and CD-1 nude mouse strains as determined by ICP-MS. Data are displayed as mean ± standard deviation with a sample size of $n = 3–4$. (C) Hepatobiliary elimination pathway of nanoparticles: Following intravenous injection, nanoparticles first go to the liver, then to the gallbladder, then into the intestines, and then finally out of the body *via* feces.

allowed us to trace their elimination trajectory. AuNPs of different sizes—4, 15, 50, 100, and 200 nm—were synthesized using previously established methods (Supplementary Figure S1).[17,18] AuNPs were surface modified with polyethylene glycol (PEG) and functionalized with Alexa Fluor 750 (AF750) using NHS-ester conjugation chemistry as previously described by our group.[19] After synthesis, these nanoparticles were characterized by transmission electron microscopy (TEM), dynamic light scattering (DLS), and UV−vis spectroscopy. Fluorescence of the nanoparticles was characterized by gel electrophoresis and fluorescence imaging (Supplementary Figure S2). The characterization data are presented in Figure 1 and Supplementary Table T1.

We next wanted to evaluate if intravenously administered AuNPs were present throughout the hepatobiliary elimination pathway as reported in literature. To outline the hepatobiliary elimination pathway in BALB/c mice, we used indocyanine green (ICG) as a positive control, since it is an FDA-approved tracer for hepatobiliary clearance.[20] We administered 50 nm AuNPs coated with AF750 and PEG (denoted as AF750-PEG-AuNPs) in BALB/c mice and compared their biodistribution with ICG. We observed strong accumulation of AF750-PEG-AuNP fluorescence signal in the liver (Supplementary Figure S3) and intestines (Figure 2A) in the first 4 h post-injection (HPI). The ICG signal biodistribution was different than AuNPs and suggested that nanoparticles undergo hepatobiliary elimination differently than ICG. We also confirmed using TEM analysis that AuNPs existed along the hepatobiliary pathway: in the liver, bile (from gallbladder), intestines, and feces. The TEM micrographs showed that the core of AuNPs remained intact and maintained their size along the hepatobiliary transit pathway (Supplementary Figures S4 and S5). Next, we collected the feces daily from BALB/c mice and two other commonly used mouse strains for nanomedicine and immunology studies (C57BL/6 and CD-1 nude) injected with AuNPs. We performed elemental analysis by inductively coupled plasma mass spectrometry (ICP-MS) to confirm that AuNPs were excreted out of the body. Over 14 days, 0.2−1.0% of the injected dose (ID) of AuNPs cleared through the feces (Figure 2B). These results confirmed that AuNPs can go through the canonical hepatobiliary pathway (*i.e.*, liver, gallbladder, intestines, and feces) for elimination (Figure 2C).

Why Is Such a Small Amount of AuNPs Eliminated from the Body? A key question is: Why does <1% of the injected dose of AuNPs get excreted from the body? We hypothesized that liver nonparenchymal cells, such as Kupffer

DOI: 10.1021/acsnano.9b01383
ACS Nano 2019, 13, 5785−5798

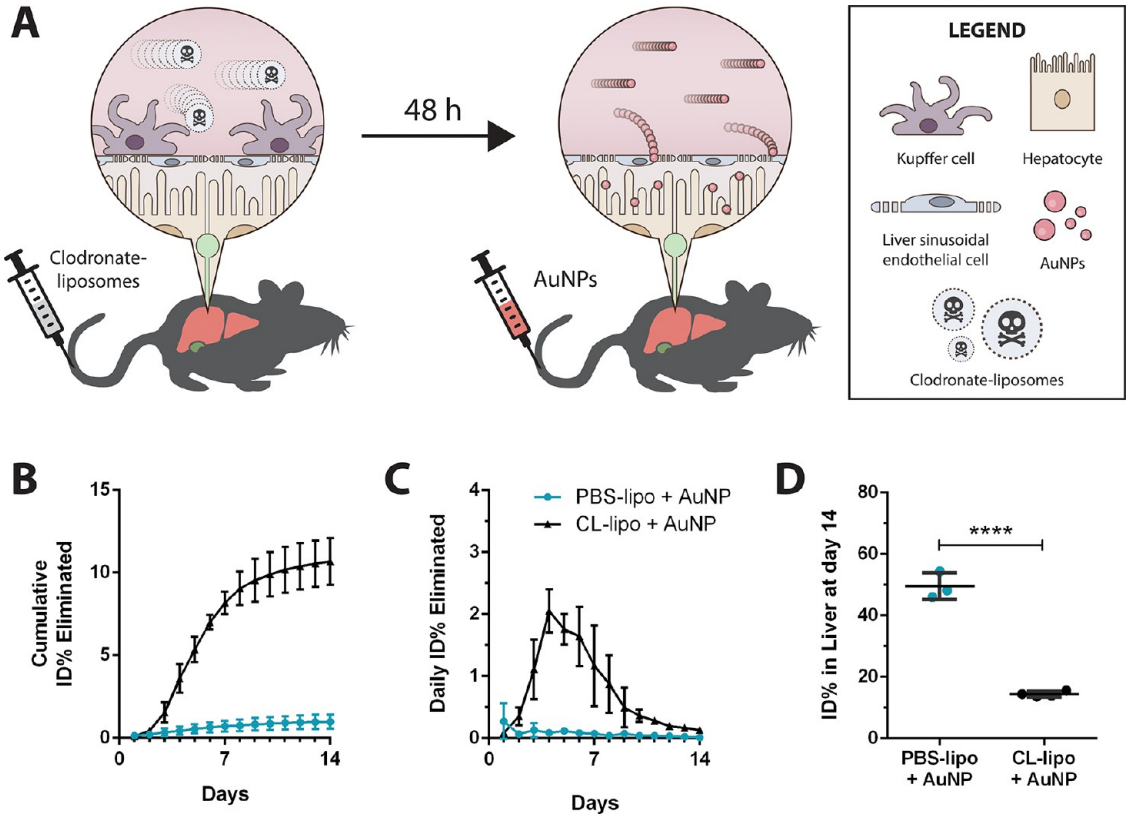

Figure 3. Kupffer cells prevented nanoparticle hepatobiliary elimination. (A) Schematic of the predepletion experiment design to investigate Kupffer cells and nanoparticle hepatobiliary elimination. BALB/c mice were injected with clodronate-liposomes (CL-lipo) or PBS-liposomes (PBS-lipo) first and then injected with 50 nm AuNPs 48 h after. (B) Cumulative ID% eliminated from BALB/c mice over 14 days after intravenous administration of 50 nm AuNPs. (C) Daily rate of ID% eliminated from BALB/c mice over 14 days after intravenous administration of 50 nm AuNPs. (D) ID% of the liver at the end of the experiment from BALB/c mice (14 days after intravenous administration of 50 nm AuNPs). Data are displayed as mean ± standard deviation with a sample size of $n = 3-4$. Statistics determined by unpaired t test with **** = $p < 0.0001$.

cells, act as barriers to sequester AuNPs and prevent them from entering the space of Disse. We tested this hypothesis by injecting clodronate-liposomes into BALB/c mice to remove the majority of Kupffer cells in the liver, followed by administration of 50 nm AuNPs 2 days later (Figure 3A). 50 mg/kg of clodronate-liposomes administered intravenously depleted 90% of Kupffer cells after 2 days and prevented their repopulation for up to 7 days.[21,22] Mice in the Kupffer cell depletion group eliminated more than 10 times the amount compared to the control group, 10.7% ID *vs* 1.0% ID in 14 days (Figure 3B). The daily rate of hepatobiliary elimination increased significantly starting 3 days post-injection of nanoparticles (Figure 3C). Elimination peaked on day 4 and decreased gradually to nondepleted rates by the end of the experiment period on day 14. There was no change to the amount of feces produced by mice in both control and clodronate-liposome treatment groups throughout the 14 days (Supplementary Figure S6). The improvement in hepatobiliary elimination was accompanied by a substantial decrease in liver accumulation of AuNPs (Figure 3D) and redistribution to other organs including the spleen and small intestines (Supplementary Figure S7). Specifically, there was 14.4% ID in the liver on day 14 for Kupffer cell depleted mice compared to approximately 49.5% ID for control mice. We did not achieve 100% elimination of the administered AuNPs. The likely explanation is that nanoparticles interacted with other nonparenchymal liver cells that were not depletable by clodronate-liposomes.

We further verified that Kupffer cells impeded the elimination of AuNPs by sequestration using histology and electron microscopy. We performed immunohistochemistry and dark-field imaging of liver histological sections to investigate AuNP distribution in the livers of Kupffer cell depleted and control mice 24 h after AuNP administration (Figure 4A). Histology showed that F4/80$^+$ Kupffer cell populations disappeared in depleted livers (Figure 4B). No gross inflammation was observed from clodronate-liposome treatment. Other hepatic cell populations also did not seem to be affected (Supplementary Figure S8). Dark-field imaging of control livers showed that AuNPs were primarily in or associated with Kupffer cells and negligibly in any other hepatic cell types in control mice. In Kupffer cell depleted livers, the AuNP signal was more diffused and could be observed in the liver sinusoidal endothelium as well as in the space of Disse and hepatocytes. We quantified the localization of AuNPs with respect to the sinusoidal borders as defined by CD209b$^+$ liver sinusoidal endothelial cells using sgementation by Ilastik and image analysis by FIJI (Supplementary Figure S9).[23,24] We found that when Kupffer cells were removed, the average dark-field intensity signal from the AuNPs in the extravascular region of the liver increased by approximately 45% (Figure 4C). We followed up with TEM studies to visualize the subcellular localization of AuNPs in the Kupffer cell depleted liver at 4, 24, 48, and 72 h post-injection of AuNPs. Kupffer cell depletion resulted in greater frequency of AuNPs in hepatocytes and the space of Disse (Figure 4D). We

DOI: 10.1021/acsnano.9b01383
ACS Nano 2019, 13, 5785−5798

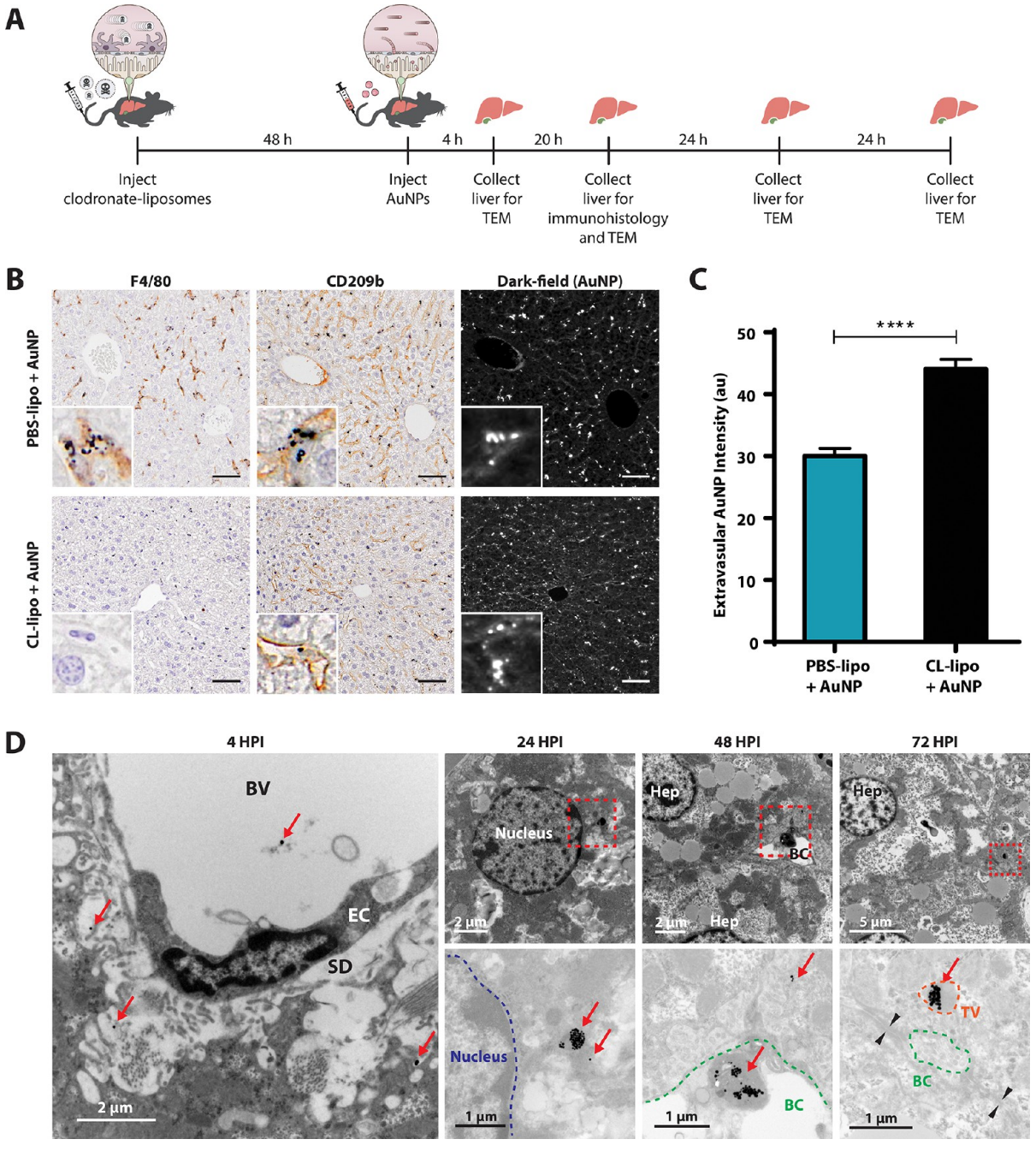

Figure 4. Kupffer cell depletion improvednanoparticle biliary access. (A) Schematic of the predepletion experiment design to investigate nanoparticle biliary access. (B) Immunohistological sections at 10× magnification of control PBS-liposome (PBS-lipo) pretreated and clodronate-liposome (CL-lipo) pretreated BALB/c mice livers 24 h post-injection with 50 nm AuNPs; stained with F4/80 antibody (for Kupffer cells), CD209b antibody (for liver sinusoidal endothelial cells), and imaged with dark-field microscopy (for visualization of 50 nm AuNPs); inlays are 40× magnification of a liver sinusoid in the section. Scale bars are 50 μm. (C) Quantification of AuNP dark-field intensity of immunohistological liver sections from (B) extravascular to the liver sinusoidal endothelium based on CD209b staining. (D) Representative TEM images of livers from BALB/c mice pretreated with clodronate-liposomes at 4, 24, 48, and 72 h post-injection of 50 nm AuNPs. Bottom panels for 24, 48, and 72 h post-injection are magnified regions of the corresponding areas indicated by the red dotted squares. Red arrows indicate locations of nanoparticles. Black triangle pairs indicate the occluding belt between adjacent hepatocytes. BV = blood vessel, EC = endothelial cell, SD = space of Disse, BC = bile canaliculus, TV = transport vesicle, Hep = hepatocyte. Data are displayed as mean ± standard deviation with a sample size of n = 3−4. Statistics determined by unpaired t test with **** = $p < 0.0001$.

observed multiple instances of AuNP transport in hepatocytes toward or into the bile canaliculi at 48 HPI and 72 HPI (Figure 4D). In contrast, AuNPs in control mice were overwhelmingly inside Kupffer cells and not in the space of Disse nor hepatocytes up to 14 days post-injection of AuNPs (Supplementary Figure S10). This agreed with our previous studies, which had found no measurable amounts of nanoparticles in hepatocytes when the nonparenchymal cells were present.[13,25] Incidentally, the dose of AuNP administered in this study is optimized for reliable elemental analyses by ICP-MS (Supplementary Figure S11) and was approximately 4−5 times higher than our previous studies.

DOI: 10.1021/acsnano.9b01383
ACS Nano 2019, 13, 5785−5798

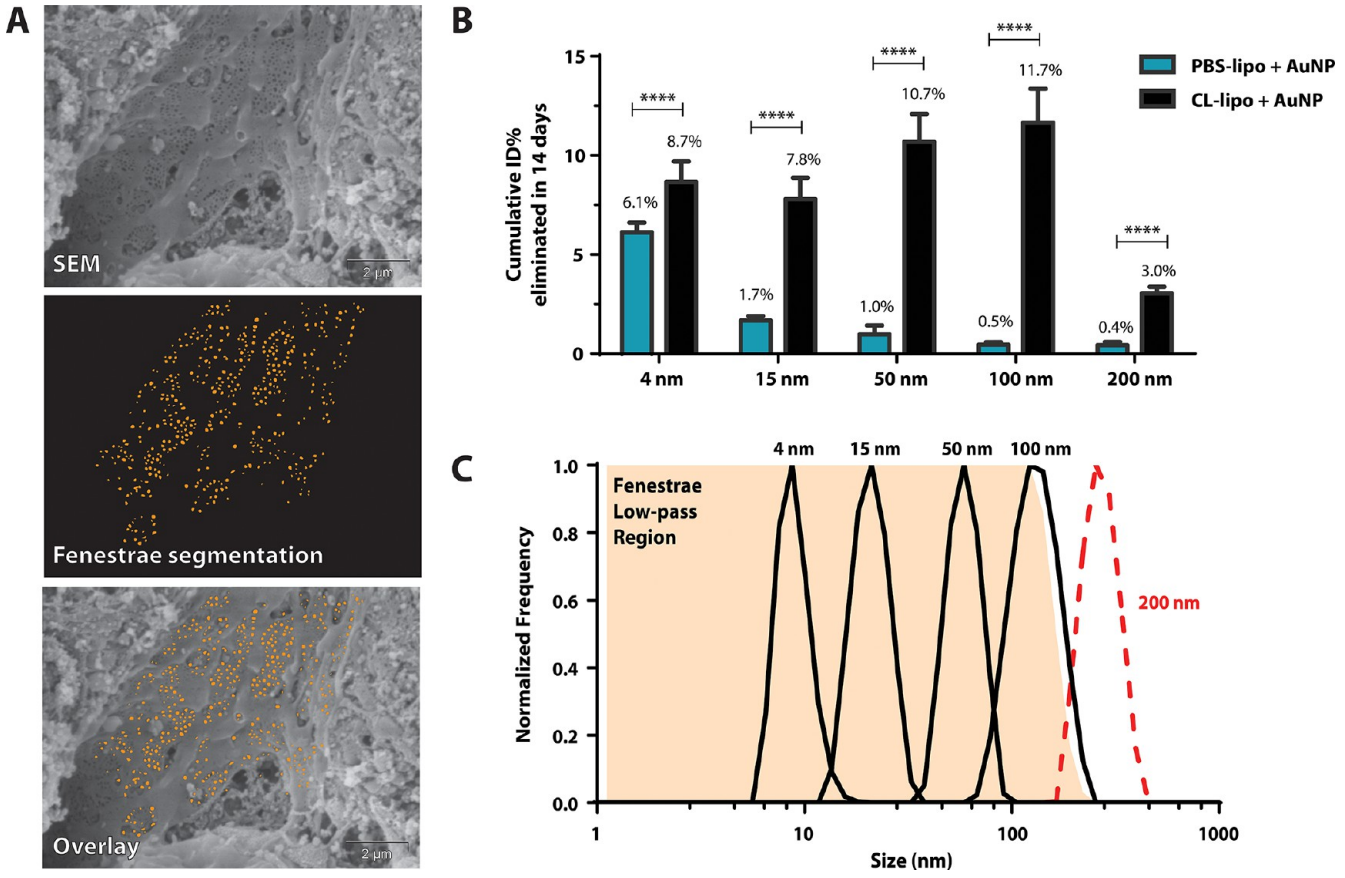

Figure 5. Liver sinusoidal endothelial cell fenestrae impeded AuNP hepatobiliary elimination based on size. (A) Representative scanning electron micrograph and segmentation of a control BALB/c mouse liver sinusoid. (B) Cumulative ID% eliminated from BALB/c mice for 14 days after intravenous administration of different sized AuNPs with and without Kupffer cell predepletion. (C) Normalized frequency distributions of the hydrodynamic diameter of 4, 15, 50, 100, and 200 nm AuNPs overlaid with the measured liver sinusoidal endothelial cell fenestrae size distribution as a low-pass filter (orange shaded area). Data are displayed as mean ± standard deviation with a sample size of $n = 3–4$. Statistics determined by unpaired t test with **** = $p < 0.0001$.

To further investigate the importance of liver nonparenchymal cells in mediating nanoparticle hepatobiliary elimination, we devised a "jailbreak" approach where we removed Kupffer cells after they had first taken up AuNPs. In this jailbreak experiment, we first administered AuNPs to mice and then administered clodronate-liposomes to deplete Kupffer cells and free their sequestered nanoparticles 7 days later (Supplementary Figure S12A). We hypothesized that this approach would flood the liver sinusoid locally with AuNPs and allow them to access the hepatobiliary pathway more easily. Contrary to our hypothesis, we found that fewer AuNPs could be eliminated out from mice using this jailbreak approach (2.3% ID) in comparison to the clodronate-liposome predepletion approach (10.7% ID) (Supplementary Figure S12B). The maximum daily rate of AuNP elimination after jailbreak was also lower than the predepletion approach (0.4% ID/day *vs* 2.1% ID/day) (Supplementary Figure S12C). In addition, there was no difference in the liver accumulation of AuNPs between control and jailbroken mice on day 14 (Supplementary Figure S12D). Blood pharmacokinetics of AuNPs showed that they did not circulate long in the blood after being freed from Kupffer cells (Supplementary Figure S13) and were most likely retaken up by other hepatic cells in the liver sinusoid.[26,27] These results suggested to us that other liver nonparenchymal cells are also important in influencing AuNP hepatobiliary transit in the sinusoid.

Role of Nanoparticle Size in Hepatobiliary Elimination. Since we observed nanoparticles to cluster around liver sinusoidal endothelial cells, we next sought to determine how these cells influenced nanoparticle hepatobiliary elimination. Fenestrae in liver sinusoidal endothelial cells control the porosity of the liver endothelium and physically regulate access of lipoproteins and viruses to hepatocytes.[28,29] We hypothesized that in Kupffer cell depleted livers, the liver sinusoidal endothelial cell fenestrae could regulate nanoparticle access to hepatocytes in a size-dependent manner. First, we performed scanning electron microscopy (SEM) on livers to observe its sinusoid luminal topography. We observed distinct, well-organized, and similarly sized fenestrae in the liver sinusoid endothelium of both control and Kupffer cell depletion groups (Figure 5A and Supplementary Figure S14).[30] We quantified that the Feret diameter (maximum distance between any points on the perimeter) of liver sinusoidal endothelial cell fenestrae was 103 ± 23 nm in BALB/c mice using segmentation by Ilastik and image analysis by FIJI.[23,24] As a reference, the liver sinusoidal endothelial cell fenestrae size in humans was reported to be 107.5 ± 1.5 nm.[29]

This led us to hypothesize that smaller nanoparticles would have better access to the space of Disse and therefore experience greater elimination. We repeated similar experiments to the 50 nm AuNPs for the 4, 15, 100, and 200 nm AuNPs. The dose of nanoparticles was normalized by surface area to be the same as

DOI: 10.1021/acsnano.9b01383
ACS Nano 2019, 13, 5785–5798

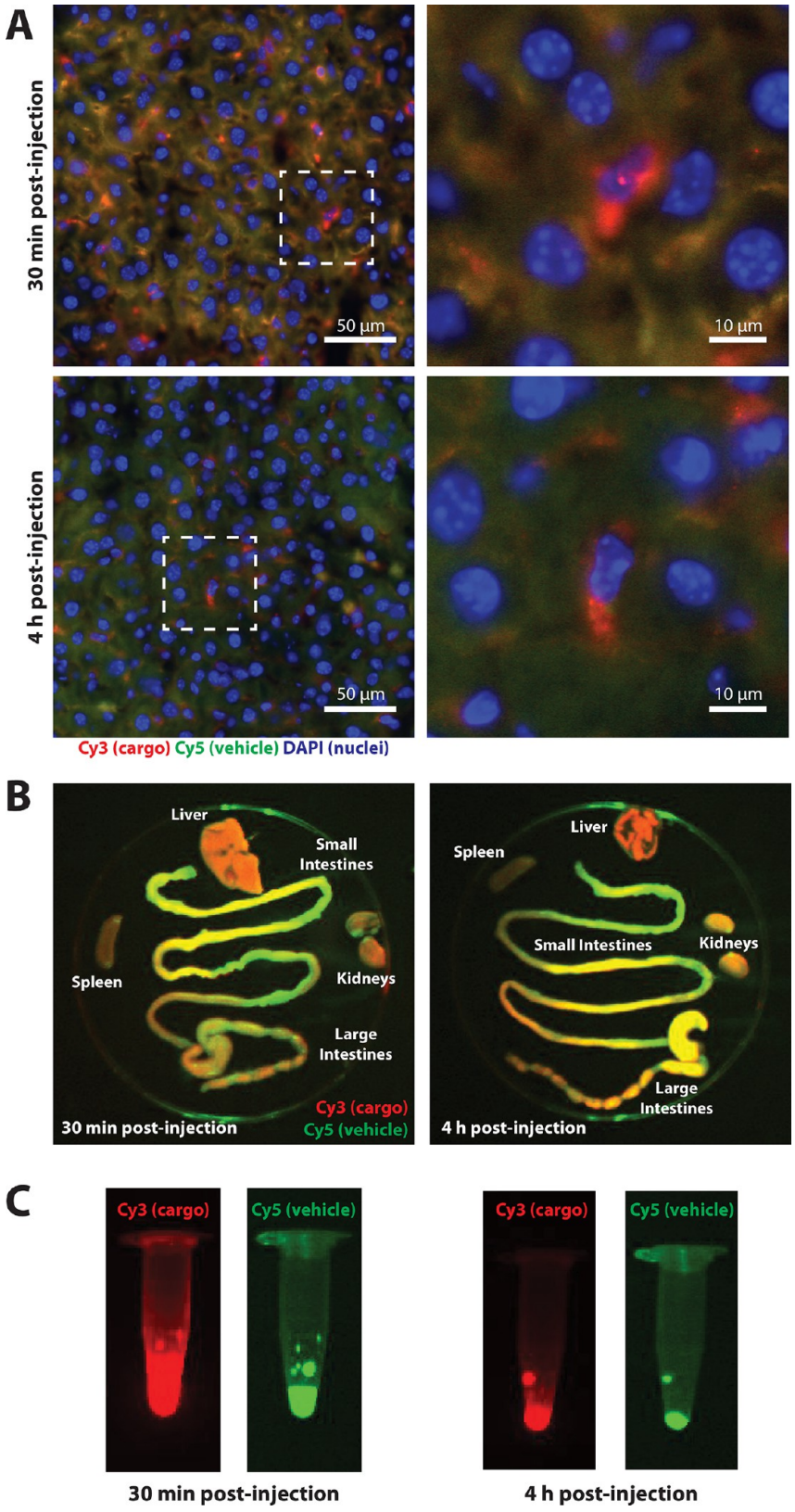

Figure 6. Biodegradable dual-labeled liposomes are eliminated as breakdown products. (A) Fluorescence imaging micrographs of cryo-frozen liver sections at 20× magnification from BALB/c mice 30 min and 4 h post-injection of dual-labeled liposomes. Right panels are enlarged sections of the boxed region from the left panel. (B) *Ex vivo* whole organ fluorescence imaging of liver, kidneys, spleen, and gastrointestinal tract from BALB/c mice 30 min and 4 h post-injection of dual-labeled liposomes. (C) Fluorescence imaging of urine collected from BALB/c mice 30 min and 4 h post-injection of dual-labeled liposomes. In all images, blue denotes DAPI staining, red denotes Cy3 (liposome 10 kDa dextran cargo), and green denotes Cy5 (lipid component of liposome).

DOI: 10.1021/acsnano.9b01383
ACS Nano 2019, 13, 5785−5798

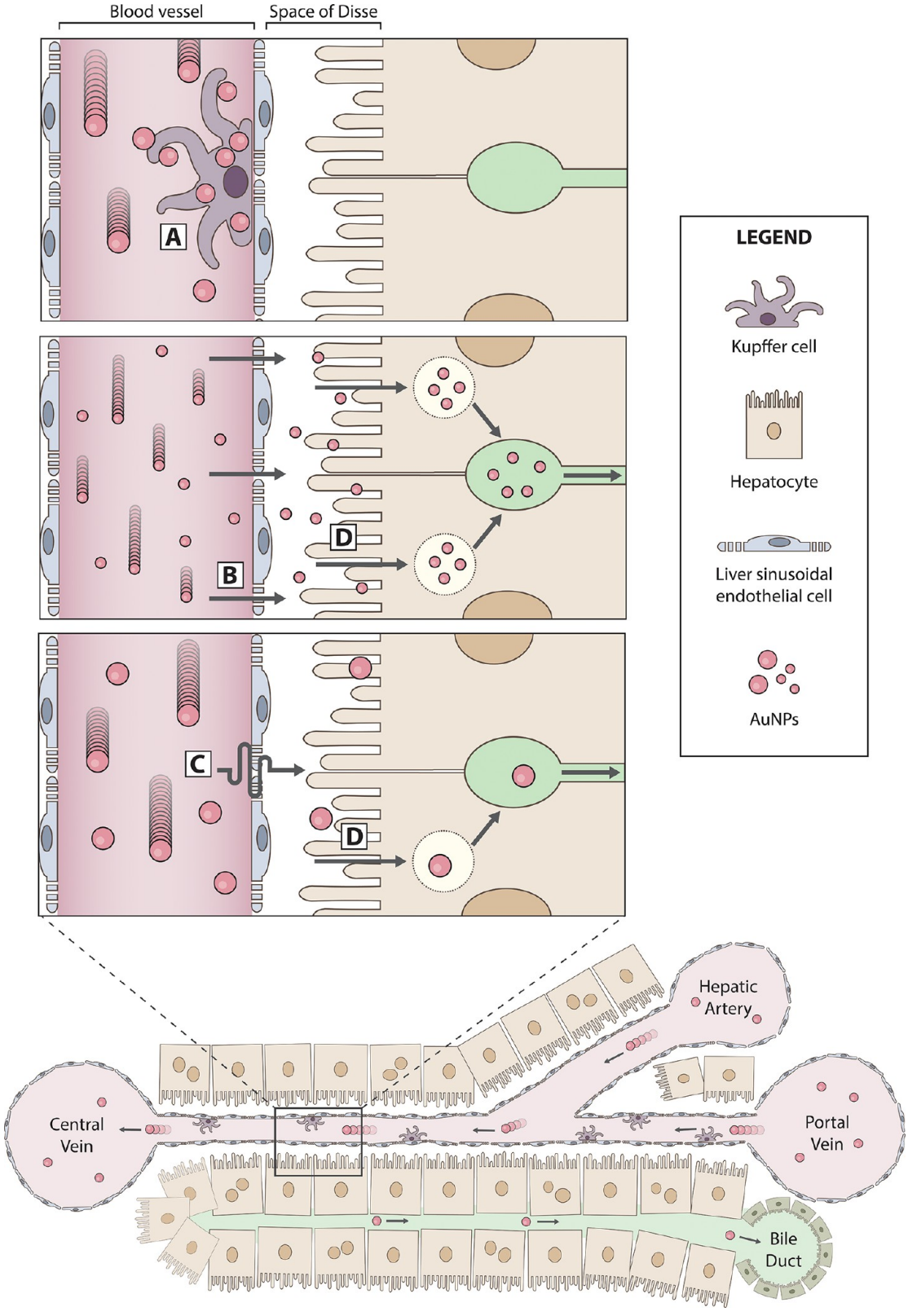

Figure 7. Proposed mechanism of nonbiodegradable nanoparticle hepatobiliary elimination in the liver sinusoid. Nanoparticles injected intravenously enter the liver and into the liver sinusoid. (A) Kupffer cells take up the majority of circulating nanoparticles based on size. Kupffer cells prefer to sequester larger nanoparticles than smaller nanoparticles. (B) If Kupffer cells are removed from the sinusoid, then nanoparticles can exit the liver sinusoidal endothelium more efficiently. (C) Larger nanoparticles may become impeded by the fenestrae size limit of the liver sinusoidal endothelial cell. (D) Nanoparticles then collect in the space of Disse, where hepatocytes slowly take them up and process them for transport into the bile canaliculus. Nanoparticles then transit out of the liver into the intestines and eventually out of the body *via* feces.

DOI: 10.1021/acsnano.9b01383
ACS Nano 2019, 13, 5785−5798

the 50 nm AuNPs. We reasoned that nanoparticle interaction with liver cells occurred at the nanoparticle surface and constant surface area would be the best dose normalization metric across different nanoparticle sizes.[31] We observed a clear size-dependent effect for cumulative fecal elimination over 2 weeks for control and predepleted groups (Figure 5B and Supplementary Figure S15). Similarly, we observed a redistribution of gold from the liver to other organs, including the spleen, small intestines, and kidneys in a size-dependent manner (Supplementary Figure S16). In control groups, 200 nm AuNPs eliminated the least efficiently (0.4% ID), whereas 4 nm AuNPs eliminated the most efficiently (6.1% ID). There was a decreasing exponential relationship (Supplementary Figure S17) between hepatobiliary elimination efficiency (ID%) and AuNP diameter (d_{AuNP}), defined by eq 1:

$$\mathrm{ID\%} = 9.989e^{-0.149d_{AuNP}} + 0.604 \quad (1)$$

Kupffer cells are more effective in the phagocytosis of larger nanoparticles and not as efficient at removing small nanoparticles from sinusoidal circulation.[31−33] We hypothesized that smaller AuNPs have higher hepatobiliary elimination because they would have greater opportunity to extravasate out of the liver endothelium to interact with hepatocytes. Our TEM studies showed that as the AuNP size increased, their frequency in the space of Disse decreased even though we still observed large AuNPs in hepatocytes and liver sinusoidal endothelial cells (Supplementary Figures S18 and S19).

In clodronate-liposome treated groups, AuNP hepatobiliary elimination efficiency increased significantly for all AuNP sizes tested. The 100 nm AuNPs exhibited the greatest degree of increase (~25 times) and greatest absolute magnitude of hepatobiliary elimination (11.7% ID). There was a slight increasing trend for the absolute ID% of hepatobiliary elimination as AuNP size increased in predepleted mice, but this trend stopped suddenly for 200 nm AuNPs. We hypothesized that the relatively low hepatobiliary elimination of 200 nm AuNPs even in the clodronate-liposome treated mice was because they were too large to physically diffuse through liver sinusoidal endothelial cell fenestrae to the space of Disse. In other words, the liver sinusoidal endothelial cells acted as a low-pass filter that excluded or impeded the extravasation of AuNPs larger than their fenestrae size (Figure 5C). There was still improvement to the hepatobiliary elimination after Kupffer cell depletion because the circulation half-life of the 200 nm AuNPs increased drastically.[22,34] Furthermore, 200 nm AuNPs were found inside liver sinusoidal endothelial cells by TEM (Supplementary Figure S20), which might suggest that their access to hepatocytes was indirect and contributed by transcytosis through liver sinusoidal endothelial cells as opposed to directly *via* liver sinusoidal endothelial cell fenestrae. Our results implicated both Kupffer cells and liver sinusoidal endothelial cells in being responsible for the size-dependent hepatobiliary elimination of AuNPs.

What Is the Difference in Hepatobiliary Elimination of Biodegradable Nanocarriers and Nonbiodegradable Nanoparticles? We next wanted to compare the elimination of biodegradable nanocarriers and nonbiodegradable nanoparticles. We hypothesized that in contrast to the nonbiodegradable AuNPs, biodegradable nanocarriers (such as liposomes) could break down into their constituent materials and undergo elimination as small molecules. We synthesized 100 nm dual-labeled liposomes—the lipid membrane was covalently labeled with Cy5 and the liposome encapsulated Cy3-labeled 10 kDa dextran (Supplementary Figure S21)—as model biodegradable nanocarriers. We intravenously injected the dual-labeled liposomes into BALB/c mice and performed *ex vivo* fluorescence imaging of the major organs and collected urine to track their *in vivo* degradation and biodistribution. In our images, Cy3 (cargo) is pseudocolored red, and Cy5 (liposome vehicle) is pseudocolored green. Intact liposomes have colocalized Cy3 and Cy5 fluorescence, which appear as yellow.

At 30 min post-injection, liposomes were mostly intact *in vivo* as evidenced by large areas of yellow in the fluorescence imaging of liver histology sections (Figure 6A). At 4 HPI, there was less yellow area, indicating that liposomes had begun to degrade. We also observed the emergence of distinct red-colored cells at both time points. We identified these red-colored cells as Kupffer cells by their morphology, as they are relatively small (5−10 μm in diameter), noncuboidal, and have distinctive small noncircular nuclei. This indicated that Kupffer cells most likely contributed to the degradation of liposomes, which had been reported by other research groups previously.[35,36] The degradation products of the liposome had different cellular localization: Cy3-dextran associated with Kupffer cells, while the Cy5-labeled lipids were found more ubiquitously in other hepatic cells. We tracked the transit of the degradation products out of the mice using *ex vivo* fluorescence imaging (Figure 6B). Red fluorescence dominated in the liver, which supported our observations that the Cy3-dextran accumulated in Kupffer cells. Along the intestines, there were distinct regions of noncolocalized Cy3 and Cy5 fluorescence signal at both 30 min and 4 h post-injection, which suggested that liposome degradation products transit differently in the gastrointestinal tract for fecal elimination. Cy3 and Cy5 fluorescence signal was also detected in the urine collected at 30 min and 4 h post-injection (Figure 6C). Together, these results demonstrated that the elimination of biodegradable nanocarriers occurred differently than nonbiodegradable nanoparticles because their degradation products could efficiently undergo renal and hepatobiliary elimination.

CONCLUSIONS AND OUTLOOK

In this study, we identified and quantified the cellular obstacles for nonbiodegradable nanoparticle hepatobiliary elimination in the context of the liver sinusoid using AuNPs as model nonbiodegradable nanoparticles (Figure 7). Liver nonparenchymal cells, namely Kupffer cells and liver sinusoidal endothelial cells, were the major culprits in causing the low intrinsic and variable hepatobiliary elimination of nonbiodegradable nanoparticles. The majority of intravenously administered nanoparticles were associated with these nonparenchymal cells because they are the first liver cells to interact with nanoparticles and have high phagocytic ability for nanoparticles. These cells prevented nanoparticle transport out of the liver sinusoidal endothelium and restricted nanoparticle access to the space of Disse to interact with hepatocytes. There are fenestrae in the liver sinusoid by which the nanoparticles transport through to the space of Disse. The sizes of these fenestrae vary between animal species.[28] Particles with dimensions that are larger than these fenestrae cannot directly enter the space of Disse, but may access it by a less efficient and slower process *via* transcytosis through the liver sinusoidal endothelial cells.[37−39] These are the first "barriers" to prevent the interaction of nonbiodegradable nanoparticles with hepatocytes. Future studies need to focus more deeply on the nanoparticle biotransformation and *in vivo* interaction with hepatocytes, bile ducts, and intestines, as all of these biological components

DOI: 10.1021/acsnano.9b01383
ACS Nano 2019, 13, 5785−5798

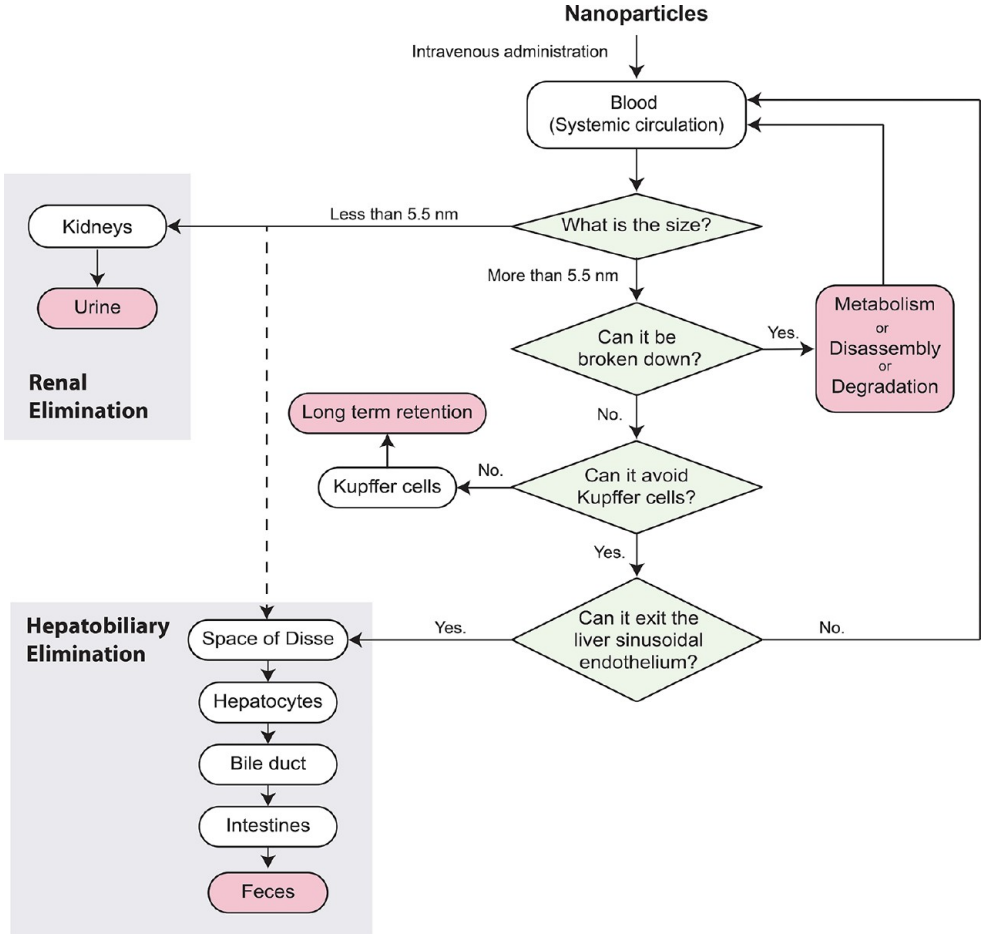

Figure 8. Decision making flowchart for nanoparticle fate *in vivo*.

can further influence their elimination efficiency and rate. Our findings suggest that the cellular physiology of the liver acts as a multilayered gatekeeper system with built-in redundancy that can compensate for one another to restrict access of the hepatobiliary pathway for large and nonbiodegradable nanoparticles. The pathway is different between biodegradable nanocarriers and nonbiodegradable nanoparticles.

The long-term fate and toxicity of retained nonbiodegradable nanoparticles in the body remains unclear and somewhat controversial as there is no consensus of the results.[40,41] Given our results and those of prior studies on nanoparticle excretion, we can start to build the bigger picture of how nanoparticles are eliminated from the body. This can enable researchers to start to manipulate cell types and cellular processes in the elimination pathway to push clinical translation of nonbiodegradable nanoparticles forward. Previous studies have focused on renal elimination, and we have begun to develop a better understanding of how to design efficient renally clearable nanomedicines.[18,42,43] However, as of now, the pathway for nonrenally clearable nanomedicines remains unsubstantiated. Here, we propose an *in vivo* decision tree of how nanoparticles are eliminated (Figure 8). Most nanoparticles less than the glomerular filtration size limit (~5.5 nm) undergo renal elimination by the kidneys and leave the body *via* the urine.[6] In our studies here, we also observed there to be fecal elimination for these small nanoparticles. Biodegradable nanocarriers or nanoparticles that are larger than 5.5 nm can be disassembled, broken down,[44,45] or metabolized[46,47] and may return to the systemic circulation. The majority of nonbiodegradable nanoparticles larger than 5.5 nm become retained long-term in Kupffer cells.[27] If Kupffer cells can be avoided or if Kupffer cells are incapacitated, then the nanoparticles may undergo hepatobiliary elimination. Akin to the glomerular filtration size limit, we propose there is a liver sinusoidal endothelial cell fenestrae filtration size limit. Nanoparticles larger than the liver sinusoidal endothelial cell fenestrae size have restricted access to hepatocytes, while the smaller nanoparticles have better access *via* fenestrae to enter the space of Disse. Overall, nanoparticles need to escape these barriers established by liver nonparenchymal cells before they have the potential to enter the space of Disse and interact with hepatocytes for elimination. Once nanoparticles successfully interact with hepatocytes, they may transcytose through to enter the bile ducts. Eventually, the nanoparticles enter the intestines and are removed from the body *via* feces. Further studies can start to fill in this decision tree with greater precision. A higher resolution map of the hepatobiliary elimination pathway will guide the design of medically useful nanoparticles.

MATERIALS AND METHODS

Materials and Reagents. All buffers and reagent solutions were prepared using purified deionized water with resistivity of 18.2 MΩ·cm at 25 °C. 10× phosphate buffered saline (PBS) solution and 10× tris-borate EDTA (TBE) buffer were obtained from Bio Basic Canada Inc. (Markham, ON). PBS buffers were autoclaved before use. Gold(III) chloride trihydrate ($HAuCl_4 \cdot 3H_2O$) (99.9% trace metals basis), sodium citrate tribasic dihydrate (99.0% ACS grade), hydroquinone

DOI: 10.1021/acsnano.9b01383
ACS Nano 2019, 13, 5785−5798

(99.5% ReagentPlus), sodium bicarbonate (99.7% ACS grade), agarose (low EEO), chloroform (>99% anhydrous), tannic acid (ACS grade), potassium carbonate (≥99.0%), bis(*p*-sulfonatophenyl)-phenylphosphine dihydrate dipotassium salt (BSPP) (97%), and indocyanine green (Cardiogreen, polymethine dye) were purchased from Sigma-Aldrich (Oakville, ON) and used without further purification. Alexa Fluor 750 succinimidyl ester (AF750-NHS ester) was purchased from Invitrogen (ThermoFisher Scientific, Carlsbad, CA). Sulfo-Cyanine3 succinimidyl ester (Cy3-NHS), sulfo-Cyanine5 succinimidyl ester (Cy5-NHS), and dibenzocyclooctyne-PEG4-maleimide (DBCO-PEG4-Mal) were purchased from Click Chemistry Tools (Scottsdale, AZ). Methoxy-PEG-thiol (550 Da), methoxy-PEG-thiol (5 kDa), and amino-PEG-thiol (10 kDa) were purchased from Nanocs Inc. (New York, NY), Laysan Bio, Inc. (Arab, AL), and Rapp Polymere (Tübingen, Germany), respectively. Tween 20 (biotechnology grade), 4-(2-hydroxyethyl)-1-piperazineethanesulfonic acid (HEPES) (biotechnology grade), and sodium chloride (reagent grade) were purchased from BioShop Canada Inc. (Burlington, ON). 10 kDa amino-dextran is purchased from Fina Biosolutions LLC (Rockville, MD). 1,2-Distearoyl-*sn*-glycero-3-phosphocholine (DSPC) and cholesterol were purchased from Avanti Polar Lipids (Alabaster, AL). 1,2-Distearoyl-*sn*-glycero-3-phosphatidylethanolamine-*N*-[azido(polyethylene glycol)-2000] (DSPE-$PEG_{2\ kDa}$-Azide) was purchased from Creative Enzymes (Shirley, NY). CKKKKKKK-peptide was purchased from Biomatik (Cambridge, ON). Clodronate-liposomes (5 mg/mL suspension) and PBS-liposomes were purchased from Liposoma BV (Amsterdam, The Netherlands).

Animal Care. All animal procedures were performed in compliance with protocols approved by the University of Toronto Division of Comparative Medicine and associated animal care committee (protocol numbers: 20010886, 20011520, 20011962, and 20011605). Six-week-old female CD-1 nude, C57BL/6, and BALB/c mice were purchased from Charles River Laboratories. Mice were acclimatized for 1 week following delivery.

Synthesis and Functionalization of AuNPs. 4 nm AuNPs were synthesized from the reduction of $HAuCl_4$ (10% w/v) by trisodium citrate (2% w/v), tannic acid (2% w/v), and potassium carbonate (50 mM). Bis(*p*-sulfonatophenyl)phenylphosphine dihydrate dipotassium salt (BSPP, 80 mg/mL) was added to the nanoparticle solution as a surface modification agent to improve colloidal stability. The 15 nm AuNPs were synthesized as per Frens' method.[48] The 50, 100, and 200 nm AuNPs were synthesized by seed-mediated growth using Perrault's method.[17] Nanoparticles were characterized by transmission electron microscopy (TEM), dynamic light scattering (DLS) (Malvern Instruments), and UV−visible absorbance spectroscopy (Shimadzu Scientific Instruments). Functionalization of AuNPs was performed as described previously by Tavares *et al.*[22] Briefly, AuNPs were centrifuged and washed twice with 0.02% (w/v) sodium citrate. The 15, 50, 100, and 200 nm AuNPs were resuspended in deionized water containing a mixed poly(ethylene) glycol (PEG) solution of 10 kDa amino-PEG-thiol (NH_2-$PEG_{10\ kDa}$-SH) and 5 kDa methoxy-PEG-thiol (CH_3O-$PEG_{5\ kDa}$-SH) at a mole ratio of 1:4 and a final concentration of 4 PEG/nm^2. The 4 nm AuNPs were resuspended in deionized water containing 550 Da methoxy-PEG-thiol (CH_3O-$PEG_{550\ Da}$-SH) at a concentration of 4 PEG/nm^2. The mixed PEG film was left to graft onto nanoparticles for 1 h in a 60 °C water bath. PEGylated nanoparticles were centrifuged and washed twice in 0.1 M sodium bicarbonate solution (pH 8.4). Next, AF750-NHS ester dye was reacted overnight on an agitator protected from light with PEGylated 15, 50, 100, and 200 nm nanoparticles in 2-fold molar excess of the initial NH_2-$PEG_{10\ kDa}$-SH amount in 0.1 M sodium bicarbonate solution. All functionalized AuNPs were washed once in 0.1 M sodium bicarbonate solution, once in 1× sterile PBS containing 0.05% v/v Tween-20, and twice in sterile 1× sterile PBS. Functionalization of AuNPs were confirmed by gel electrophoresis using 0.5× TBE 1% agarose gel run at 135 V for 60 min and fluorescence imaging with Kodak multispectral imaging system (Bruker Corporation).

Synthesis of Dual-Labeled Liposomes. Liposomes were prepared using 1,2-distearoyl-*sn*-glycero-3-phosphocholine (DSPC), cholesterol, and 1,2-distearoyl-*sn*-glycero-3-phosphatidylethanolamine-*N*-[azido(polyethylene glycol)-2000] (DSPE-$PEG_{2\ kDa}$-Azide) in a molar ratio of 55:40:5 (DSPC:cholesterol:DSPE-$PEG_{2\ kDa}$-Azide). Lipids were dissolved and mixed in chloroform. Chloroform was removed by evaporation using a rotary evaporator to create a lipid thin film prior to additional freeze-drying overnight. Lipid films were resuspended in a solution of 3.3 mg/mL Cy3-dextran in 1× PBS. Cy3-dextran was prepared by reaction between 10 kDa amino-dextran and Cy3-NHS at a ratio of 4:1 in 100 mM HEPES buffer at pH 8.5 overnight. Cy3-dextran was purified by ethanol precipitation and washing in a 3 kDa Amicon filter three times. The mixture underwent 5 freeze/thaw cycles with liquid nitrogen and a 60 °C water bath and was then manually extruded with a 100 nm filter under 60 °C heating 21 times. Liposomes were then purified using a size exclusion column (NAP5, GE Healthcare). Following purification, 0.5 mg dibenzocyclooctyne-PEG-maleimide (DBCO-PEG4-Mal) suspended in 1× PBS was added to the lipid mixture. DBCO-PEG-Mal underwent a copper-free click chemistry reaction with available azide groups for 45 min. Excess DBCO-PEG-Mal was removed by washing the mixture three times in a 100 kDa Amicon filter with 1× PBS. Next, 0.5 mg of peptide (sequence C−N terminus: CKKKKKKK) and 0.5 mg of Cy5-NHS suspended in 1× PBS was added to the mixture and incubated at room temperature for 3 h in the dark. Excess peptide and Cy5-NHS were removed using size exclusion column (NAP5) and further purified by washing in a 100 kDa Amicon filter. When free Cy5 was no longer being removed from the mixture (∼5 washes), liposomes were reconstituted back to the initial solution volume.

Administration of ICG, AuNPs, Clodronate-Liposomes, PBS-Liposomes, and Dual-Labeled Liposomes. For imaging studies, mice were administered indocyanine green (ICG) in 1× sterile PBS intravenously *via* tail vein using a 29-gauge insulin needle at a dose of 5 mg ICG per kg and fixed volume of 150 μL. For AuNP imaging, biodistribution, and TEM studies, mice were injected with 4, 15, 50, 100, and 200 nm AuNPs at a fixed volume of 150 μL intravenously *via* the tail vein using a 29-gauge insulin needle. The injected dose between different nanoparticle sizes was normalized to the total nanoparticle surface area, 1.42×10^{16} nm^2. We approximated the AuNPs as spheres, so the corresponding concentrations for 4, 15, 50, 100, and 200 nm AuNPs administered were 3125, 222.2, 20, 5, and 1.25 nM, respectively. For Kupffer cell depletion studies, mice were injected intravenously *via* the tail vein with 50 mg/kg of clodronate-liposome suspension or PBS-liposome suspension using a 29-guage insulin needle (usually approximately 200 μL). For dual-labeled liposome imaging studies, mice were injected with a dose of 750 mg lipid per kg in a volume of 150 μL.

***Ex Vivo* Fluorescence Imaging of ICG and AuNP Biodistribution.** Following administration of ICG, dual-labeled liposomes, or AF750-PEG-AuNPs, mice were euthanized at the indicated time points. Mice were perfused using 4% paraformaldehyde in 1× PBS to remove residual blood and prevent excessive auto fluorescence during imaging. Organs were excised, further washed with 1× PBS, and placed onto Petri dishes. *Ex vivo* fluorescence imaging was performed using a Kodak *in vivo* multispectral imaging system (Bruker Corporation) at indicated time points. Imaging of the organs used the following combination of excitation and emission bandpass filters and integration times: Cy3 (550 nm excitation/600 nm emission/1 min integration time); Cy5 (650 nm excitation/700 nm emission/1 min integration time); AF750 (750 nm excitation/830 nm emission/2 min integration time); and ICG (750 nm excitation/850 nm emission/2 min integration time). The bandpass of each filter was ∼35 nm at fwhm (Carestream Health). Fluorescence images were modified using FIJI for intensity normalization and background subtraction.

Collection of Feces. Following administration of AuNPs, mice were singly housed and kept under light−dark cycles with 12 h of light and 12 h of darkness per day. Mice had free access to water and food. Feces was collected daily from each cage manually during the light cycle.

Quantitative Determination of AuNPs in Organs and Feces by ICP-MS. Organs (including heart, lungs, liver, spleen, stomach, small intestine, large intestine, and kidneys) and feces were collected as

DOI: 10.1021/acsnano.9b01383
ACS Nano 2019, 13, 5785−5798

described above. Samples were weighed and placed into glass culture tubes (VWR International Co). 0.20−0.25 g of feces from each mouse per day per test condition was used for quantitative analysis. 800 μL of 69% (w/v) ACS-grade hydrochloric acid (Caledon Laboratories Limited) was added to each sample and left to digest overnight in a 70 °C water bath. The next morning, 200 μL of 37% (w/v) ACS grade hydrochloric acid was added to each sample and further left to digest for 3 h. Digested samples were then diluted using deionized water to a final volume of 40 mL (or a final acid concentration of 2% v/v HNO_3 and 0.5% v/v HCl). Next, diluted samples were filtered using a 0.22 μm PES syringe filter (EMD Millipore-Merck). A calibration curve was also prepared ranging from 0.0001 to 100 μg/mL using elemental gold standard solution (High-Purity Standards). Quantitative determination of gold content was performed on a NexION 350Q ICP-MS (PerkinElmer) at the University Health Network Nanomedicine Fabrication Center (NanoMed Fab). Iridium was used as an internal standard with the mass analyzer set to ^{197}Au for gold quantification and ^{192}Ir for internal standard quantification. Total gold content in organs was normalized as a percentage of the injected dose. Gold content in blood was normalized as a percentage of the injected dose in the collected weight of blood and then re-adjusted to 1.8 g (the average total blood content of a 20 g mouse). Gold content in feces was normalized as a percentage of the injected dose to the digested weight of feces (typically 0.20−0.25 g) and then re-adjusted to the total collected weight of feces (typically 0.50−1.00 g).

Immunohistochemistry and Histological Tissue Analysis. Sections of the liver were fixed in 10% neutral buffered formalin (Sigma-Aldrich) for 24 h or frozen with frozen section compound (VWR International, LLC) and liquid nitrogen. The fixed tissues were then sent to the Toronto Centre for Phenogenomics (TCP) for further histological processing. Tissue sections were stained for hepatic macrophages using anti-F4/80 antibody (ab6640, Abcam), for liver sinusoidal endothelial cells using anti-CD209b (eBio22D1, eBioscience), and for hepatic B cells using anti-B220 (103247, BioLegend). Tissue sections are then counter-stained with DAPI or hematoxylin and eosin. Stained liver slices were imaged as full slide scans by TCP. CD209b immunohistology images were segmented for liver sinusoids using Ilastik to define intravascular and extravascular regions of the liver. MATLAB was used to calculate the mean nanoparticle intensity from dark-field imaging of each defined region. MATLAB code is available at: https://github.com/BenKingston/Histology_Liver_NP_Int_WP

Transmission Electron Microscopy. Sections of the liver and intestines were immersion fixed with 0.5% formaldehyde, 4% glutaraldehyde in 1× PBS at room temperature for 1 h, and then overnight at 4 °C. Fixed tissues were then sent to The Hospital for Sick Children Nanoscale Biomedical Imaging Facility for further processing. Bile from the gallbladder was collected from euthanized mice using a 29-gauge insulin needle. Bile was then diluted using Milli-Q ultrapure water at a ratio of 1:10. Feces samples were mechanically broken up and sonicated in Milli-Q ultrapure water, then filtered through a 0.22 μm PES syringe filter (EMD Millipore-Merck). Bile and feces samples were then blotted onto a plasma treated TEM grid (Ted Palla, Inc.) and left to air-dry. Imaging of bile samples was performed using the Hitachi H-7000 conventional TEM at the University of Toronto Centre for Nanostructure Imaging. Imaging of prepared tissue samples and feces was performed using a Tecnai F20 microscope at ABC.

Scanning Electron Microscopy. Sections of the liver were immersion fixed with 0.5% formaldehyde, 4% glutaraldehyde in 1× PBS at room temperature for 1 h, and then overnight at 4 °C. Fixed tissues were then sent to The Hospital for Sick Children Advanced Bioimaging Centre (ABC) for gold sputter coating. Imaging of liver samples was performed using the Philips XL30 ESEM at ABC with an electron beam spot size of 3 at 10 kV. Images were segmented for fenestrae using Ilastik, and fenestrae Feret diameter is obtained from the "Analyze Particles" built-in function of FIJI.

Statistical Analyses. Data were analyzed by unpaired *t* tests using GraphPad Prism 6 unless otherwise specified. Data are presented as average values of the stated number of replicates, and precision is presented as sample standard deviation, unless otherwise stated. Statistical significance between experimental groups and conditions is given as **p*-value < 0.05, ***p*-value < 0.01, ****p*-value < 0.001, and *****p*-value < 0.0001.

ASSOCIATED CONTENT

Supporting Information

The Supporting Information is available free of charge on the ACS Publications website at DOI: 10.1021/acsnano.9b01383.

Figures S1−S21 and Table T1 (PDF)

AUTHOR INFORMATION

Corresponding Author

*E-mail: warren.chan@utoronto.ca.

ORCID

Wilson Poon: 0000-0003-2192-3077

Stefan Wilhelm: 0000-0003-2167-6221

Warren C. W. Chan: 0000-0001-5435-4785

Author Contributions

◆Y.-N.Z. and B.O. contributed equally. W.P. and W.C.W.C. conceptualized the project. W.P., Y.-N.Z., B.O., and J.L.Y.W. designed and performed nanoparticle synthesis and biodistribution/elimination experiments. W.P., Y.-N.Z., and S.W. performed electron microscopy experiments. W.P., Y.-N.Z., and B.R.K. designed and performed fluorescence imaging experiments. W.P. and B.R.K. designed and automated analyses of histological sections to quantify nanoparticle localization and electron microscopy images to characterize fenestrae. W.P. performed formal data analysis. W.C.W.C. acquired funding for this project. W.P. and W.C.W.C. designed visualizations of this submission. W.P. and W.C.W.C. wrote the initial manuscript draft. All authors contributed to review and editing of the manuscript.

Notes

The authors declare no competing financial interest.

ACKNOWLEDGMENTS

The authors thank S.A. MacParland, W. Ngo, D.K. Zhang, Z.P. Lin, and J.C. Senécal for fruitful discussions; A.M. Syed, P. MacMillan, and J. Ngai for donating the dual-labeled liposomes; M. Ganguly at the Toronto Centre for Phenogenomics for his assistance with histology; and D. Holmyard at the Nanoscale Biomedical Imaging Facility for his expertise in electron microscopy. W.P. acknowledges CIHR, OGS, Barbara and Frank Milligan, and Cecil Yip for provision of fellowships and graduate scholarships. Y.-N.Z. thanks NSERC, OGS, Wildcat Foundation, and Paul and Sally Wang for provision of fellowships and graduate scholarships. B.O. thanks the Vanier Canada Graduate Scholarship, CIHR, the McLaughlin Centre for MD/PhD studentships, and the Donnelly Centre for graduate fellowships. B.R.K. thanks NSERC, Wildcat Foundation, and the Donnelly Centre for student scholarships, and the Royal Bank of Canada (RBC) for graduate fellowship. J.L.Y.W. thanks Barbara and Frank Milligan for provision of graduate fellowship. Graphical abstract was designed using resources from Freepik.com. W. C.W. C. would like to acknowledge CIHR (FDN-159932; MOP-130143), NSERC (2015-06397), Canadian Research Chairs program (950-223824), CHRP program (CPG-146468), and Canadian Cancer Society (705185-1) for funding support.

DOI: 10.1021/acsnano.9b01383
ACS Nano 2019, 13, 5785−5798

REFERENCES

(1) Choi, H. S.; Frangioni, J. V. Nanoparticles for Biomedical Imaging: Fundamentals of Clinical Translation. *Mol. Imaging* **2010**, *9*, 291−310.

(2) Alkilany, A. M.; Murphy, C. J. Toxicity and Cellular Uptake of Gold Nanoparticles: What We Have Learned So Far? *J. Nanopart. Res.* **2010**, *12*, 2313−2333.

(3) Kim, S.; Lim, Y. T.; Soltesz, E. G.; De Grand, A. M.; Lee, J.; Nakayama, A.; Parker, J. A.; Mihaljevic, T.; Laurence, R. G.; Dor, D. M.; Cohn, L. H.; Bawendi, M. G.; Frangioni, J. V. Near-Infrared Fluorescent Type II Quantum Dots for Sentinel Lymph Node Mapping. *Nat. Biotechnol.* **2004**, *22*, 93−97.

(4) Wang, S.; Ma, X.; Hong, X.; Cheng, Y.; Tian, Y.; Zhao, S.; Liu, W.; Tang, Y.; Zhao, R.; Song, L.; Teng, Z.; Lu, G. Adjuvant Photothermal Therapy Inhibits Local Recurrences After Breast-Conserving Surgery with Little Skin Damage. *ACS Nano* **2018**, *12*, 662−670.

(5) Zhang, Y.-N.; Poon, W.; Tavares, A. J.; McGilvray, I. D.; Chan, W. C. W. Nanoparticle−Liver Interactions: Cellular Uptake and Hepatobiliary Elimination. *J. Controlled Release* **2016**, *240*, 332−348.

(6) Soo Choi, H.; Liu, W.; Misra, P.; Tanaka, E.; Zimmer, J. P.; Itty Ipe, B.; Bawendi, M. G.; Frangioni, J. V. Renal Clearance of Quantum Dots. *Nat. Biotechnol.* **2007**, *25*, 1165−1170.

(7) Du, B.; Yu, M.; Zheng, J. Transport and Interactions of Nanoparticles in the Kidneys. *Nat. Rev. Mater.* **2018**, *3*, 358−374.

(8) Yu, M.; Xu, J.; Zheng, J. Renal Clearable Luminescent Gold Nanoparticles: From the Bench to the Clinic. *Angew. Chem., Int. Ed.* **2019**, *58*, 4112−4128.

(9) Soji, T.; Murata, Y.; Ohira, A.; Nishizono, H.; Tanaka, M.; Herbert, D. C. Evidence That Hepatocytes Can Phagocytize Exogenous Substances. *Anat. Rec.* **1992**, *233*, 543−546.

(10) Ogawara, K.-I.; Yoshida, M.; Furumoto, K.; Takakura, Y.; Hashida, M.; Higaki, K.; Kimura, T. Uptake by Hepatocytes and Biliary Excretion of Intravenously Administered Polystyrene Microspheres in Rats. *J. Drug Targeting* **1999**, *7*, 213−221.

(11) Grislain, L.; Couvreur, P.; Lenaerts, V.; Roland, M.; Deprez-Decampeneere, D.; Speiser, P. Pharmacokinetics and Distribution of a Biodegradable Drug-Carrier. *Int. J. Pharm. (Amsterdam, Neth.)* **1983**, *15*, 335−345.

(12) Le Ray, A. M.; Vert, M.; Gautier, J. C.; Benoît, J. P. Fate of [14C]Poly(DL-Lactide-Co-Glycolide) Nanoparticles After Intravenous and Oral Administration to Mice. *Int. J. Pharm. (Amsterdam, Neth.)* **1994**, *106*, 201−211.

(13) Fischer, H. C.; Liu, L.; Pang, K. S.; Chan, W. C. W. Pharmacokinetics of Nanoscale Quantum Dots: *In Vivo* Distribution, Sequestration, and Clearance in the Rat. *Adv. Funct. Mater.* **2006**, *16*, 1299−1305.

(14) Liu, Z.; Davis, C.; Cai, W.; He, L.; Chen, X.; Dai, H. Circulation and Long-Term Fate of Functionalized, Biocompatible Single-Walled Carbon Nanotubes in Mice Probed by Raman Spectroscopy. *Proc. Natl. Acad. Sci. U. S. A.* **2008**, *105*, 1410−1415.

(15) Fu, C.; Liu, T.; Li, L.; Liu, H.; Chen, D.; Tang, F. The Absorption, Distribution, Excretion and Toxicity of Mesoporous Silica Nanoparticles in Mice Following Different Exposure Routes. *Biomaterials* **2013**, *34*, 2565−2575.

(16) Liu, C.; Gao, Z.; Zeng, J.; Hou, Y.; Fang, F.; Li, Y.; Qiao, R.; Shen, L.; Lei, H.; Yang, W.; Gao, M. Magnetic/Upconversion Fluorescent NaGdF4:Yb,Er Nanoparticle-Based Dual-Modal Molecular Probes for Imaging Tiny Tumors *In Vivo*. *ACS Nano* **2013**, *7*, 7227−7240.

(17) Perrault, S. D.; Chan, W. C. W. Synthesis and Surface Modification of Highly Monodispersed, Spherical Gold Nanoparticles of 50−200 nm. *J. Am. Chem. Soc.* **2009**, *131*, 17042−17043.

(18) Chou, L. Y. T.; Zagorovsky, K.; Chan, W. C. W. DNA Assembly of Nanoparticle Superstructures for Controlled Biological Delivery and Elimination. *Nat. Nanotechnol.* **2014**, *9*, 148−155.

(19) Dai, Q.; Walkey, C.; Chan, W. C. W. Polyethylene Glycol Backfilling Mitigates the Negative Impact of the Protein Corona on Nanoparticle Cell Targeting. *Angew. Chem., Int. Ed.* **2014**, *53*, 5093−5096.

(20) Guidance for Industry Pharmacokinetics in Patients with Impaired Hepatic Function: Study Design, Data Analysis, and Impact on Dosing and Labeling. https://www.fda.gov/downloads/drugs/guidancecomplianceregulatoryinformation/guidances/ucm072123.pdf (accessed February 15, 2019).

(21) Rooijen, N. V.; Sanders, A. Liposome Mediated Depletion of Macrophages: Mechanism of Action, Preparation of Liposomes and Applications. *J. Immunol. Methods* **1994**, *174*, 83−93.

(22) Tavares, A. J.; Poon, W.; Zhang, Y.-N.; Dai, Q.; Besla, R.; Ding, D.; Ouyang, B.; Li, A.; Chen, J.; Zheng, G.; Robbins, C.; Chan, W. C. W. Effect of Removing Kupffer Cells on Nanoparticle Tumor Delivery. *Proc. Natl. Acad. Sci. U. S. A.* **2017**, *114*, E10871−E10880.

(23) Sommer, C.; Strähle, C.; Köthe, C. S. U.; Hamprecht, F. A. Ilastik: interactive learning and segmentation toolkit. Proceedings from the *Eighth IEEE International Symposium on Biomedical Imaging (ISBI)*, Chicago, Illinois, March 30−April 2, 2011; IEEE: Piscataway, NJ, 2011; pp 230−233. IEEE Xplore. http://www.ieee.org (accessed Jan 16, 2019).

(24) Schindelin, J.; Arganda-Carreras, I.; Frise, E.; Kaynig, V.; Longair, M.; Pietzsch, T.; Preibisch, S.; Rueden, C.; Saalfeld, S.; Schmid, B.; Tinevez, J.-Y.; White, D. J.; Hartenstein, V.; Eliceiri, K.; Tomancak, P.; Cardona, A. Fiji: An Open-Source Platform for Biological-Image Analysis. *Nat. Methods* **2012**, *9*, 676−682.

(25) Tsoi, K. M.; MacParland, S. A.; Ma, X.-Z.; Spetzler, V. N.; Echeverri, J.; Ouyang, B.; Fadel, S. M.; Sykes, E. A.; Goldaracena, N.; Kaths, J. M.; Conneely, J. B.; Alman, B. A.; Selzner, M.; Ostrowski, M. A.; Adeyi, O. A.; Zilman, A.; McGilvray, I. D.; Chan, W. C. W. Mechanism of Hard-Nanomaterial Clearance by the Liver. *Nat. Mater.* **2016**, *15*, 1212−1221.

(26) Park, J.-K.; Utsumi, T.; Seo, Y.-E.; Deng, Y.; Satoh, A.; Saltzman, W. M.; Iwakiri, Y. Cellular Distribution of Injected PLGA-Nanoparticles in the Liver. *Nanomedicine (N. Y., NY, U. S.)* **2016**, *12*, 1365−1374.

(27) Sadauskas, E.; Wallin, H.; Stoltenberg, M.; Vogel, U.; Doering, P.; Larsen, A.; Danscher, G. Kupffer Cells are Central in the Removal of Nanoparticles from the Organism. *Part. Fibre Toxicol.* **2007**, *4*, 10.

(28) Braet, F.; Wisse, E. Structural and Functional Aspects of Liver Sinusoidal Endothelial Cell Fenestrae: A Review. *Comp. Hepatol.* **2002**, *1*, 1.

(29) Wisse, E.; Jacobs, F.; Topal, B.; Frederik, P.; De Geest, B. The Size of Endothelial Fenestrae in Human Liver Sinusoids: Implications for Hepatocyte-Directed Gene Transfer. *Gene Ther.* **2008**, *15*, 1193−1199.

(30) Poisson, J.; Lemoinne, S.; Boulanger, C.; Durand, F.; Moreau, R.; Valla, D.; Rautou, P.-E. Liver Sinusoidal Endothelial Cells: Physiology and Role in Liver Diseases. *J. Hepatol.* **2017**, *66*, 212−227.

(31) Perrault, S. D.; Walkey, C.; Jennings, T.; Fischer, H. C.; Chan, W. C. W. Mediating Tumor Targeting Efficiency of Nanoparticles Through Design. *Nano Lett.* **2009**, *9*, 1909−1915.

(32) Hirn, S.; Semmler-Behnke, M.; Schleh, C.; Wenk, A.; Lipka, J.; Schäffler, M.; Takenaka, S.; Möller, W.; Schmid, G.; Simon, U.; Kreyling, W. G. Particle Size-Dependent and Surface Charge-Dependent Biodistribution of Gold Nanoparticles After Intravenous Administration. *Eur. J. Pharm. Biopharm.* **2011**, *77*, 407−416.

(33) Cho, W.-S.; Cho, M.; Jeong, J.; Choi, M.; Han, B. S.; Shin, H.-S.; Hong, J.; Chung, B. H.; Jeong, J.; Cho, M.-H. Size-Dependent Tissue Kinetics of PEG-Coated Gold Nanoparticles. *Toxicol. Appl. Pharmacol.* **2010**, *245*, 116−123.

(34) Shiratori, Y.; Tananka, M.; Kawase, T.; Shiina, S.; Komatsu, Y.; Omata, M. Quantification of Sinusoidal Cell Function *In Vivo*. *Semin. Liver Dis.* **1993**, *13*, 39−49.

(35) Dijkstra, J.; Van Galen, M.; Regts, D.; Scherphof, G. Uptake and Processing of Liposomal Phospholipids by Kupffer Cells *In Vitro*. *Eur. J. Biochem.* **1985**, *148*, 391−397.

(36) Daemen, T.; Velinova, M.; Regts, J.; de Jager, M.; Kalicharan, R.; Donga, J.; van der Want, J. J. L.; Scherphof, G. L. Different Intrahepatic Distribution of Phosphatidylglycerol and Phosphatidylserine Liposomes in the Rat. *Hepatology (Hoboken, NJ, U. S.)* **1997**, *26*, 416−423.

(37) Jenne, C. N.; Kubes, P. Immune Surveillance by the Liver. *Nat. Immunol.* **2013**, *14*, 996−1006.

DOI: 10.1021/acsnano.9b01383
ACS Nano 2019, 13, 5785−5798

(38) Fraser, R.; Dobbs, B. R.; Rogers, G. W. T. Lipoproteins and the Liver Sieve: The Role of the Fenestrated Sinusoidal Endothelium in Lipoprotein Metabolism, Atherosclerosis, and Cirrhosis. *Hepatology (Hoboken, NJ, U. S.)* **1995**, *21*, 863−874.
(39) Steffan, A.-M.; Gendrault, J.-L.; McCuskey, R. S.; McCuskey, P. A.; Kirn, A. Phagocytosis, an Unrecognized Property of Murine Endothelial Liver Cells. *Hepatology (Hoboken, NJ, U. S.)* **1986**, *6*, 830−836.
(40) Falagan-Lotsch, P.; Grzincic, E. M.; Murphy, C. J. One Low-Dose Exposure of Gold Nanoparticles Induces Long-Term Changes in Human Cells. *Proc. Natl. Acad. Sci. U. S. A.* **2016**, *113*, 13318−13323.
(41) Ali, M. R. K.; Rahman, M. A.; Wu, Y.; Han, T.; Peng, X.; Mackey, M. A.; Wang, D.; Shin, H. J.; Chen, Z. G.; Xiao, H.; Wu, R.; Tang, Y.; Shin, D. M.; El-Sayed, M. A. Efficacy, Long-Term Toxicity, and Mechanistic Studies of Gold Nanorods Photothermal Therapy of Cancer in Xenograft Mice. *Proc. Natl. Acad. Sci. U. S. A.* **2017**, *114*, E3110−E3118.
(42) Chen, F.; Ma, K.; Madajewski, B.; Zhuang, L.; Zhang, L.; Rickert, K.; Marelli, M.; Yoo, B.; Turker, M. Z.; Overholtzer, M.; Quinn, T. P.; Gonen, M.; Zanzonico, P.; Tuesca, A.; Bowen, M. A.; Norton, L.; Subramony, J. A.; Wiesner, U.; Bradbury, M. S. Ultrasmall Targeted Nanoparticles with Engineered Antibody Fragments for Imaging Detection of HER2-Overexpressing Breast Cancer. *Nat. Commun.* **2018**, *9*, 4141.
(43) Wei, Q.; Chen, Y.; Ma, X.; Ji, J.; Qiao, Y.; Zhou, B.; Ma, F.; Ling, D.; Zhang, H.; Tian, M.; Tian, J.; Zhou, M. High-Efficient Clearable Nanoparticles for Multi-Modal Imaging and Image-Guided Cancer Therapy. *Adv. Funct. Mater.* **2018**, *28*, 1704634.
(44) Hwang, K. J.; Luk, K. F.; Beaumier, P. L. Hepatic Uptake and Degradation of Unilamellar Sphingomyelin/Cholesterol Liposomes: A Kinetic Study. *Proc. Natl. Acad. Sci. U. S. A.* **1980**, *77*, 4030−4034.
(45) Mohammad, A. K.; Reineke, J. J. Quantitative Detection of PLGA Nanoparticle Degradation in Tissues Following Intravenous Administration. *Mol. Pharmaceutics* **2013**, *10*, 2183−2189.
(46) Pouliquen, D.; Le Jeune, J. J.; Perdrisot, R.; Ermias, A.; Jallet, P. Iron Oxide Nanoparticles for Use as an MRI Contrast Agent: Pharmacokinetics and Metabolism. *Magn. Reson. Imaging* **1991**, *9*, 275−283.
(47) Poller, W. C.; Pieber, M.; Boehm-Sturm, P.; Ramberger, E.; Karampelas, V.; Möller, K.; Schleicher, M.; Wiekhorst, F.; Löwa, N.; Wagner, S.; Schnorr, J.; Taupitz, M.; Stangl, K.; Stangl, V.; Ludwig, A. Very Small Superparamagnetic Iron Oxide Nanoparticles: Long-Term Fate and Metabolic Processing in Atherosclerotic Mice. *Nanomedicine (N. Y., NY, U. S.)* **2018**, *14*, 2575−2586.
(48) Frens, G. Controlled Nucleation for the Regulation of the Particle Size in Monodisperse Gold Suspensions. *Nature, Phys. Sci.* **1973**, *241*, 20−22.

DOI: 10.1021/acsnano.9b01383
ACS Nano 2019, 13, 5785−5798